www.sciencemag.org/content/353/6296/aaf8988/suppl/DC1

Supplementary Materials for

Gradual caldera collapse at Bárdarbunga volcano, Iceland, regulated by lateral magma outflow

Magnús T. Gudmundsson,* Kristín Jónsdóttir, Andrew Hooper, Eoghan P. Holohan, Sæmundur A. Halldórsson, Benedikt G. Ófeigsson, Simone Cesca, Kristín S. Vogfjörd, Freysteinn Sigmundsson, Thórdís Högnadóttir, Páll Einarsson, Olgeir Sigmarsson, Alexander H. Jarosch, Kristján Jónasson, Eyjólfur Magnússon, Sigrún Hreinsdóttir, Marco Bagnardi, Michelle M. Parks, Vala Hjörleifsdóttir, Finnur Pálsson, Thomas R. Walter, Martin P. J. Schöpfer, Sebastian Heimann, Hannah I. Reynolds, Stéphanie Dumont, Eniko Bali, Gudmundur H. Gudfinnsson, Torsten Dahm, Matthew J. Roberts, Martin Hensch, Joaquín M. C. Belart, Karsten Spaans, Sigurdur Jakobsson, Gunnar B. Gudmundsson, Hildur M. Fridriksdóttir, Vincent Drouin, Tobias Dürig, Guðfinna Aðalgeirsdóttir, Morten S. Riishuus, Gro B. M. Pedersen, Tayo van Boeckel, Björn Oddsson, Melissa A. Pfeffer, Sara Barsotti, Baldur Bergsson, Amy Donovan, Mike R. Burton, Alessandro Aiuppa

*Corresponding author. Email: mtg@hi.is

Published 15 July 2016, *Science* **353**, aaf8988 (2016)
DOI: 10.1126/science.aaf8988

This PDF file includes:

Materials and Methods

Mapping of collapse

Ice surface topography was mapped 18 times in the period September 5, 2014 to June 4, 2015 (Fig. S1). An aircraft-based system (*59*) of sub-meter differential GPS and ground clearance altimeter (4.3 GHz wave, vertical elevation accuracy ±2 m) on board the survey aircraft of Isavia, the Icelandic Civil Aviation Service (*59*) provided 13 maps (Marked as FMS on Fig. S1). Survey lines were flown at 70-120 m ground clearance, measuring 4 times/sec. (at ~15 m intervals), and included coverage of the growing geothermal ice cauldrons. Comparison with kinematic GPS ground surveys in November, February and June (accuracy ±0.3 m), as well as snow temperature models and measurements show that the reflecting surface was unaffected by accumulation of winter snow and remained at the September 2014 summer surface until October, after which it gradually migrated downwards to ~1.5 m below it by February 2015. The reflecting surface probably indicates the lower boundary of the dry snow layer where snow temperature was <0°C (*60*). A subset of this data was used by Rossi et al. (*61*) to compare with Tandem-X derived maps of the subsidence for specific dates in late 2014. Optical photogrammetry maps were made using satellite data for August 28 (Spot 6 satellite), September 20 and October 10 (Pléiades satellite). Combined, the surface data provide a record of collapse volume with time (Fig. 3B). The curve in Fig. 3B is drawn using the difference of the running average of volume obtained in three adjacent surveys. The rate of volume change obtained in this way is also used in Fig. 6B. A continuously recording GPS station (BARC) was installed on the ice-surface on September 12, 2014. This station monitored the subsidence continuously for a large part of the unrest, although snow covering the antenna lead to some data gaps. A detailed ground kinematic GPS survey within and around the caldera on June 3-10, 2015 allowed the margins of collapse to be determined. Measurements of winter accumulation in the Bárdarbunga caldera in June 2015 constrained subsidence data while a glacier surface lidar map from 2011-2012 (*62*) was used as reference surface.

Radio-echo soundings (RES)

On February 3, 2015, when over 95% of the subsidence had occurred, 45 km of RES-profiles (1-5 MHz receiver bandwidth) were measured in over-snow traverses, covering about 2/3 of the caldera floor, including a large part of the subsided area. Bedrock echoes were detected for ~90% of the measurements. Along-profile bedrock echoes in length-depth coordinates were migrated (*63*) to compensate for the width of the radar beam (~200 m). Comparison of our data with previous mapping done in 1985 (*64*) indicates that the over 60 m subsidence had not caused significant changes in ice thickness; the maximum thickness observed is close to 800 meters on both occasions.

Ice flow modelling

Assuming no basal slip ($\mathbf{v}_b = 0$), ice deformation within the caldera has been computed using a Full-Stokes finite element model solving the standard equations (*65*). On the lateral boundaries of the model domain, no flow conditions (i.e. $\mathbf{v} = 0$) have been defined and the model domain chosen to be sufficiently large so that the lateral boundary conditions do not influence the ice flow within the caldera. The rate factor in Glen's flow law (*66*) has been estimated by constraining the horizontal model surface velocities to fit the measured ones at the BARC GPS station for the period September 12 to February 3. This yielded $A=1.6\ 10^{-24}$ $Pa^{-3}s^{-1}$ assuming the nonlinearity parameter in Glen's flow law to be n=3. This is somewhat stiffer than textbook values for temperate ice ($A=2.4\ 10^{-24}$ $Pa^{-3}s^{-1}$, ref. *67*) but is to be expected in a volcanic setting where the ice body contains several tephra layers. Moreover, this low value for A supports our initial assumption of no basal slip. At the basal boundary,

the post-collapse bed topography from the RES survey has been used and the surface of each model utilized the respective surface DTM implemented as a free surface within the FEM model. The ice flow modelling (Fig. S2) indicates that the ice surface subsidence was almost identical to bedrock subsidence everywhere in the caldera (error <1 m) in September-October. However, by the end of February the inflow of ice towards the bottom of the subsidence structure had resulted in uplift of about 3 m in the center and a subsidence of 1-3 m on a circle around the uplifted central part.

Lava volume and flow rate

The surface elevation of the growing Holuhraun lava flow was measured using a Theodolite from the ground in September 21 2014, and with the Isavia aircraft (see above on mapping of collapse) on November 4 and 26, December 4 and 30 and January 21, as well as later surveys in 2015. The aircraft surveys were calibrated with kinematic GPS profiling of the surface. These data give lava volumes at the time of survey, providing estimates of the average magma flow rate over periods of some weeks (Fig. 6B) and a final lava volume of 1.5±0.2 km^3. Nettleton gravity profiles obtained in September 2015 of the lava indicate average bulk lava density of 2500±100 kg m^{-3}. Using a basaltic magma density of 2750 kg m^{-3} for pressure of 300-400 MPa (*68*) the equivalent volume of magma at ~12 km depth in the crust is 1.4±0.2 km^3.

Relative locations of microearthquakes

M ≤2 earthquakes at the caldera recorded at distances <100 km between August 1 and October 17 by the Icelandic national seismic network, SIL (*69*) were relatively relocated using a standard 1D velocity model (*70*). SIL magnitudes were calculated according to Rognvaldsson and Slunga (*71*). A double-difference method was used, where absolute and relative arrival times of P and S waves determined through cross-correlation of waveforms, were inverted for best locations in multiple overlapping groups (*72*). Depth is set to zero at bedrock caldera floor (1.2 km above sea level, see Figs. 5 and 6). The relocated events roughly follow the north and south caldera rims; mostly being outside the northern rim and ~1 km inside the southern rim (Fig. 5A-B). Stability tests of relocations with subsets of events and stations indicated perturbations to event latitudes, particularly on the northern rim, probably due to slow velocities inside the caldera.

The InSAR detected subsidence associated with a M5.3 event on 18 September places the surface fault at ~2.5 km inside the pre-existing topographic northern caldera rim (Fig. S7), while the seismic epicentre location is just north of the northern caldera rim. Using the InSAR observation to locate the surface expression for the steeply outwards dipping caldera fault, the microearthquakes were shifted southward according to: *New lat = old lat * 0.883 +7.552.* The shifted locations are used in Figure 5. The shift is of the same order as the absolute error in the hypocentre locations. However, besides fitting the hypocentres to the InSAR-located fault it provides more consistency to S-P times from 82 events observed on an accelerometer at location BARC (Fig1A) from November 2014 to February 2015.

Moment tensor inversion and classification

The steady subsidence of the caldera was accompanied by a sequence of episodic M>5 earthquakes, which excited low frequency signals recorded at regional distances throughout Iceland. We performed a regional moment tensor inversion for all events with M>5, adopting a full moment tensor (MT) point source approximation, neglecting higher order moment tensor. The MT inversion (*73*) was performed by fitting full waveforms 3-component displacements at regional distances (40-200 km), in the low frequency band 0.01-0.05 Hz. We obtain centroid location, centroid depth and full MT solutions for 77 earthquakes at the

caldera and with M > 5. MTs were decomposed into double couple (DC), compensated linear vector dipole (CLVD) and isotropic (ISO) components. Since MTs mostly differ in their DC components, we classified upon the similarity of the DC orientation using a clustering algorithm (*73*) and the normalized Kagan angle (*74*) as norm.

Waveform similarity analysis and moment estimation

To extend the interpretation of source processes to smaller events, where MT inversion becomes less stable, we apply a waveform similarity analysis. The scaling of the low frequency signals of weaker events and larger ones with similar waveforms is used to infer the scalar moment of smaller events (M < 5) from the known moment of the larger ones, resulting from the MT inversion procedure. In this way, we are able to estimate scalar moments for more than 600 events (352 with Mw > 4.0), down to a magnitude of Mw 3.3. These results allow tracking of the details of the temporal evolution of the moment release.

Mechanism corrected relative location

Moment tensor inversion provides a first estimate of centroid location and depth. A more precise location can be obtained by using relative location techniques, here also favored by the high waveform similarity. However, waveform-based lag-times can be affected by the dissimilarity among waveforms for the two families of events. To overcome this problem, we corrected cross-correlation lag times, by using corrections based upon focal mechanisms. The adopted procedure includes the computation of synthetic seismograms for different observed source mechanisms, the cross-correlation of synthetic waveforms to estimate fictitious time lags due to different focal mechanisms, and the inference of a time lag correction for each possible focal mechanism pair. As a result, we improved epicentral locations for 227 events. In order to obtain absolute locations, we combine the relative centroid locations of the largest events with the new absolute epicentral locations, imposing the condition that the mean centroid locations correspond to the mean absolute locations for both the northern and the southern cluster.

Caldera-dike seismicity correlations

The histogram shown in Figure 6A is computed using a simple model using the number of dyke earthquakes in 1.5 hour bins before and after (i) 4 < M < 4.6 and (ii) M > 4.6 caldera earthquakes (61). For example, the height of the fourth bar is found by assuming that the rate of dyke earthquakes during the 1.5 hours immediately preceding an M ≥ 4.6 caldera earthquake is α times the reference rate, and estimating α with maximum likelihood, giving α =1.96. The plot can be read as, for example, the expected rate of dyke earthquakes is increased by 96% in the time interval 1.5 hours before an M ≥ 4.6 caldera earthquake.

P-values are computed with a likelihood ratio test, and the confidence intervals are likelihood based. The reference rate (equal to 1 in Fig. 6A) is the rate of earthquake occurrence in periods more than three hours before or after caldera earthquakes of size M > 4. All dyke earthquakes that fall in one of the bins of Figure 6A together with all the dyke earthquakes in the reference periods are considered. The null hypothesis is that the portion of these earthquakes that fall in the bin is binomially distributed with parameter corresponding to a constant reference rate. To minimize the effect of the varying reference rate between months, the model assumes that this holds for each calendar month, and the final likelihood used in the test is the product of the likelihoods of individual months.

GPS analysis

The high-resolution GPS time series at BARC in the center of the caldera (Fig. 3C) was obtained using RTKLIB software, processing the receiver locations every 15 seconds as kinematic baselines from the HOFN reference station in southeast Iceland. Other GPS data were analyzed using the GAMIT/GLOBK software, version 10.6 using over 100 global reference stations to evaluate site positions in the ITRF08 reference frame. For the regional network average daily station positions were estimated. For the caldera GPS station (BARC) we furthermore divided the data into eight hour sessions using a 24 hour running window of reference station and orbit data. In the processing we solve for station coordinates, satellite orbit and earth rotation parameters, atmospheric zenith delay every two hours, and three atmospheric gradients per day. The IGS08 azimuth and elevation dependent absolute phase center offsets were applied to all antennas and ocean loading was corrected for using the FES2004 model.

InSAR analysis

We utilized X-band (wavelength 3.11 cm) radar images acquired by the COSMO-SkyMed constellation and employed two-pass Interferometric Synthetic Aperture Radar (InSAR) analysis (*75*) to measure ground deformation at Bárdarbunga caldera over 24-hr periods during which large caldera earthquakes occurred. The interferograms were processed using DORIS software (*76*) and a merged LiDAR, intermediate TanDEM-X, ASTER and EMISAR DEM was used to remove topographic fringes (*77*). To account for the large changes in topography over the caldera during the eruption, we interpolated the digital elevation model, using data from the continuous GPS station located inside the caldera. The wrapped interferometric phase values were filtered using an adaptive filter (*78*) and unwrapped with SNAPHU software (*79*). The one-day interferogram spanning September 17-18, 2014 was used to infer the location of faults that slipped during this period, which included a large caldera (M5.3) earthquake (Fig. S7). We modelled the fault system as a series of 30 rectangular vertical faults (*79*) with varying strike, and estimated location, size, minimum depth beneath the surface, and slip for each segment. Note, the data could be fitted equally well with steeply dipping faults, in either direction, but we fixed them to be vertical for convenience. The southern margin did not slip in this 24-hour interval and the model therefore does not constrain the actual location of the southern caldera fault. The contracting body at the base of the fault system was also modelled as a closing rectangular dislocation with uniform contraction (*79*). We used a Markov-chain Monte Carlo approach to estimate the multivariate probability distribution for all model parameters (*80*).

Petrological analysis and thermobarometry

Major element compositions of minerals and glasses were analyzed using a JEOL JXA-8230 electron microprobe at the Institute of Earth Sciences, University of Iceland. Fluid inclusions within phenocrysts were analysed by optical microscopy and confocal Raman spectroscopy (Horiba Jobin Yvon LabRAM HR800) at the Bayerisches Geoinstitut, Bayreuth, Germany. Eruption temperatures calculated with different thermometers (*81-83*) for the erupted lava are consistently in the range 1165-1180°C, in good agreement with on-site measurements by thermal imaging cameras. Three independent thermobarometers were used to constrain the depth of magma accumulation before the onset of the eruption; *(i) Glass thermobarometry* was carried out using the fractional crystallization model of Yang et al. (*82*), which was calibrated using basaltic melt compositions, *(ii) Clinopyroxene-Liquid Thermobarometry* was carried out based on the clinopyroxene-liquid barometers published by Putirka (*84*) that rely on the pressure and temperature dependence of Fe, Mg, Al and Na partitioning between pyroxenes and coexisting melt, and *(iii) CO_2 Density Barometry* which is

based on the principle that distance between the two Raman bands of CO_2 (in the wavenumber region between 1250 and 1450 cm^{-1}) is a function of fluid density (*85*). In combination with information on the temperature of the system, the entrapment pressure can be estimated based on the equation of state of CO_2.

Subaerial gas composition analysis

The composition of the subaerial eruptive gases was measured by open-path Fourier Transform Infrared spectrometer (FTIR) (*86*) on September 3, 19, 20 and 21 using the erupting lava as an infrared radiation source, and Multi-Component Gas Analyzer System (MultiGAS) (*87*) on September 1, 21, October 8, January 26 and Feburary 6. The MultiGAS measurements were taken downwind from vent when the plume was grounded. Major element composition and wt% of volatiles of the melt were defined using the average of four clinopyroxene-hosted melt inclusions (*88, 89*) and used as input to the D-COMPRESS magma/volatile partition software (*90*). The model was run from atmospheric pressure to 600 MPa (18 km). The simulation results indicate that the sulfur reaches 1600 ppm, the highest concentrations measured in melt inclusions most representative of the pre-eruptive magma composition (*88*)~~,~~ at 470±100 MPa (14±3 km). This estimate is partly dependent on the solubility constants provided for basalt. However, it convincingly supports the petrological and geodetic estimates.

DEM modelling

We evaluated the role of pre-existing ring fault structures on the 2014-15 collapse by using the two-dimensional Distinct Element Method (DEM) software PFC 5.0 (*90*). The DEM models comprise a 40 × 25 km gravitationally-loaded assemblage of rigid circular particles that interact according to frictional-elastic contact laws (*91*). Particles have a uniform size distribution, with radii between 60 m and 100 m, and a density of 2700 kgm^{-3}. The model's basal and the lateral boundaries are frictionless rigid walls. Inter-particle and particle-wall contacts have a Young's modulus of 70 GPa and a normal to shear stiffness ratio of 2.5. The model comprises three regions (Fig. 5D): (i) A laccolith-like 'magma reservoir'. (ii) A fault-bound reservoir 'roof'. (iii) The 'host rock' around the reservoir and roof. Within the reservoir, the contact friction is 0.01 and particles are not bonded. Outside the reservoir, the contact friction coefficient is 0.5 and particles are bonded with linear elastic beams. Bond tensile and shear strengths are 35 MPa in the roof and 70 MPa in the surrounding host rock. Note that fracturing of the weaker 'roof' zone will reduce the assembly-scale strength and modulus here, locally by up to an order of magnitude (*27*), as suggested for Bardabunga by Riel et al. (*32*). Pre-existing faults, extending from the lateral edges of the reservoir to a few kilometres below the surface (Fig. 5D), are modelled by using a contact law for 'smooth' discontinuities in poly-disperse particle assemblages (*92*). The normal and shear stiffness of these 'fault' contacts is 60 GPa/m. Withdrawal of magma is assumed to occur laterally out of the 2D model plane (Fig. 5D) and is simulated by slowly reducing the areas of the reservoir particles. Displacements of surface particles were smoothed by a standard moving mean method to minimize localized particle effects. Our modelling comprised a series of forward simulations in which the dip of each fault was varied between 80-90 degrees, initial fault depths varied from 1-3 km, and chamber width varied from 7.0-8.5 km. Chamber depth was fixed at 12 km, based on the geobarometry data, to reduce the parameter space. The lateral position of the chamber was allowed to vary depending on the fault geometry, so that the faults lay within the clouds of hypocentres and projected upward to within the caldera. Effects of Young's modulus, strength and fault friction were also systematically tested. Further details on DEM modelling of caldera collapse are given in Holohan et al. (*27*, *93*).

Geodetic depth model

To determine the approximate depth of the magma chamber, we modelled post-rifting InSAR and GPS data (Fig. S3) using a point pressure source in an elastic halfspace (*94*). The depth range at 95% confidence is 8-12 km.

Coupled caldera subsidence and eruption model

We assume piston failure occurs approximately at a constant stress threshold, causing the pressure at the top of magma chamber to remain constant on average. Therefore, we ignore compressibility and assume that the density of the magma remains constant. The driving overpressure is then given by

$$\Delta P = \frac{W-F}{A} + \rho g h - \rho g d \quad (1),$$

where W is the weight of the piston, F is the resistive force (friction), A is the cross sectional area of the magma chamber, ρ is the density of the magma, g is gravitational acceleration, h is the height of magma above the chamber exit point and d is the depth of the chamber exit point relative to the eruption site (Ext. Data 7). Conservation of mass implies

$$A\frac{dh}{dt} = -\pi r^2 v \quad (2),$$

where v is the mean magma flow speed and r is conduit radius. Assuming that the time-averaged resistive force due to friction, F, and d remain constant, differentiating (1) and substituting (2) gives

$$\frac{d\Delta P}{dt} = -\rho g \frac{\pi r^2}{A} v \quad (3).$$

Assuming pressure loss due to viscous drag from laminar flow in a cylindrical pipe (Hagen Poiseuille flow) and dynamic pressure loss on exit

$$\Delta P = \frac{8\eta L}{r^2} v + \frac{\rho}{2} v^2 \quad (4)$$

$$\Longrightarrow v = -\frac{8\eta L}{\rho r^2} + \sqrt{\left(\frac{8\eta L}{\rho r^2}\right)^2 + 2\frac{\Delta P}{\rho}} \quad (5).$$

We assume a cylindrical pipe, as models of thermal erosion predict that the cross section of a magma flow channel will evolve to be circular in shape, but note that for a non-circular cross section, the first term will still be proportional to the velocity, but with a different constant.

Expanding (5) gives

$$\Longrightarrow v = -\frac{8\eta L}{\rho r^2} + \frac{8\eta L}{\rho r^2} + \frac{r^2 \Delta P}{8\eta L} + O\left(\frac{r^2}{\eta L}\right)^2 = \frac{r^2 \Delta P}{8\eta L} + O\left(\frac{r^2}{\eta L}\right)^2 \quad (6).$$

Substituting (6) into (3) gives

$$\frac{d\Delta P}{dt} = -\frac{\pi \rho g r^2}{A}\left[\frac{r^2 \Delta P}{8\eta L} + O\left(\frac{r^2}{\eta L}\right)^2\right] \quad (7).$$

When $L >> r^2$, this reduces to

$$\frac{d\Delta P}{dt} = -\frac{\pi\rho g r^4}{8A\eta L}\Delta P \quad (8)$$

$$\Longrightarrow \Delta P = \Delta P_0 e^{-\frac{\pi\rho g r^4}{8A\eta L}t} \quad (9)$$

and

$$h - h_\infty = (h_0 - h_\infty)e^{-\frac{\pi\rho g r^4}{8A\eta L}t} \quad (10).$$

A similar relationship has been derived to explain gravity-driven eruptions at Stromboli (*95*). Assuming that $h_0 - h_\infty$ is equal to the subsidence measured at the BARC GPS station, a best fit solution is $h_0 - h_\infty$ = 67.5 m and $\frac{\pi\rho g r^4}{8A\eta L} = 1.5 \times 10^{-7}$ (Fig. 3B). A similar fit is obtained for magma flow rate and caldera volume change in Fig. 6B. Substituting ρ = 2700 kgm^{-3} (ref. *64*), g = 9.8 ms^{-2}, L = 47 km and ν=22 Pa s using the average glass compositions of the Holuhraun lava (*96*), gives ΔP_0 = 1.7 MPa and $\frac{r^4}{A} = 1.5 \times 10^{-5}$ m^2. Constraining the eruption rate to be 250 m^3/s on 31 August, gives A= 32 km^2 and r = 4.7 m. This can be considered the effective radius of the flow path assuming circular cross sectional area. A similar relation would hold for other possible geometrical forms of the flow path cross sectional area. Theoretically, the eruption would approach equilibrium (ΔP=0 in (1)) asymptotically, but choking of the conduit due to cooling, slow-moving magma is expected before that.

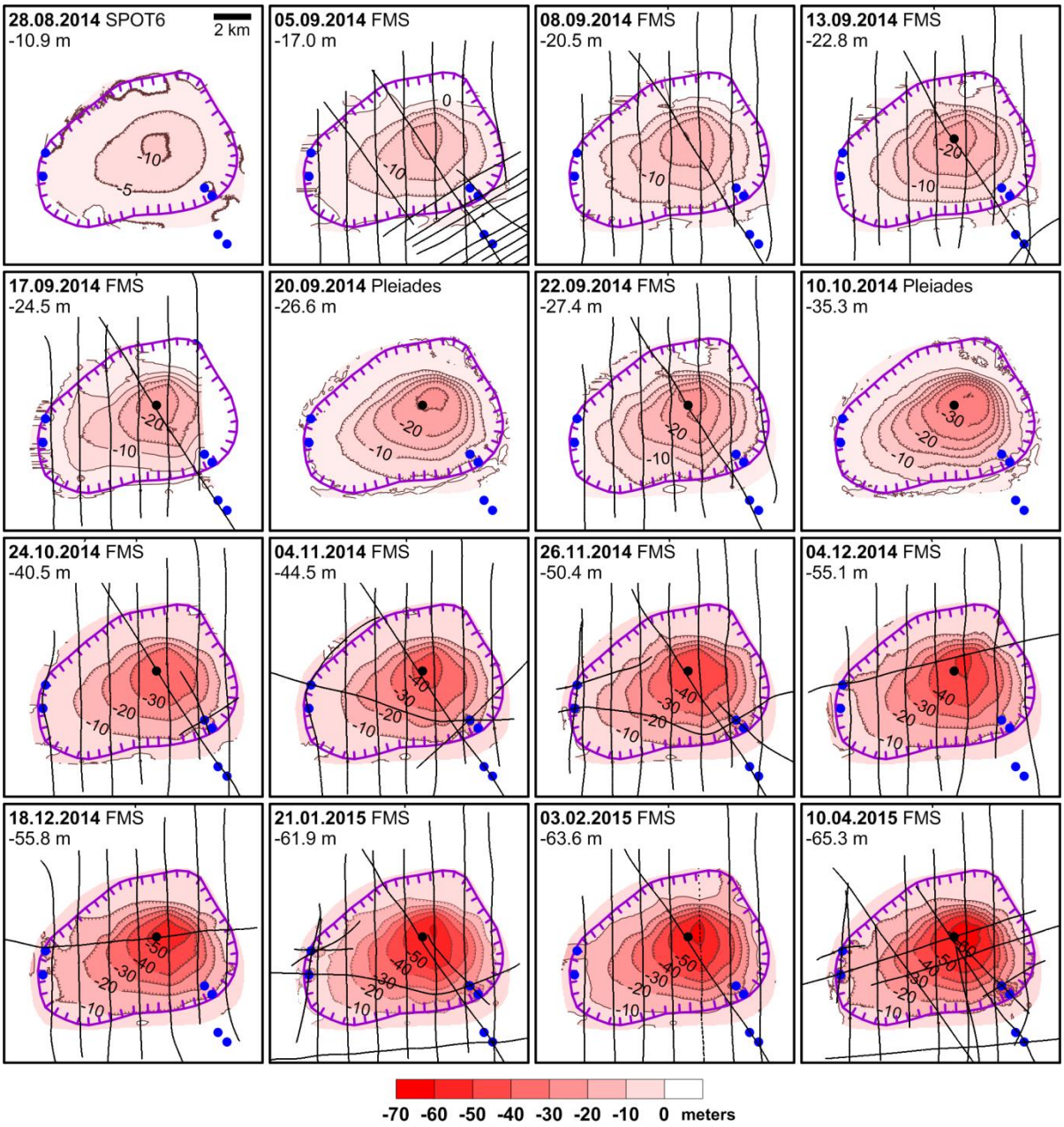

Fig. S1.

Maps of collapse – margins as in Fig. 1C. The maps are corrected for ice flow (Fig. S2) and migration of reflector into the autumn 2014 surface due to propagation of cold wave into the firn in October-April (24). The number underneath the date gives the maximum subsidence. Three maps are obtained through satellite photogrammetry (28.08 – Spot 6, 20.09 and 10.10 from Pléiades) while the remaining 13 maps (marked as FMS) are obtained using an aircraft-combining radar altimetry and a submeter Differential GPS; the maps are made by interpolation between the profiles (shown as black lines)(24).

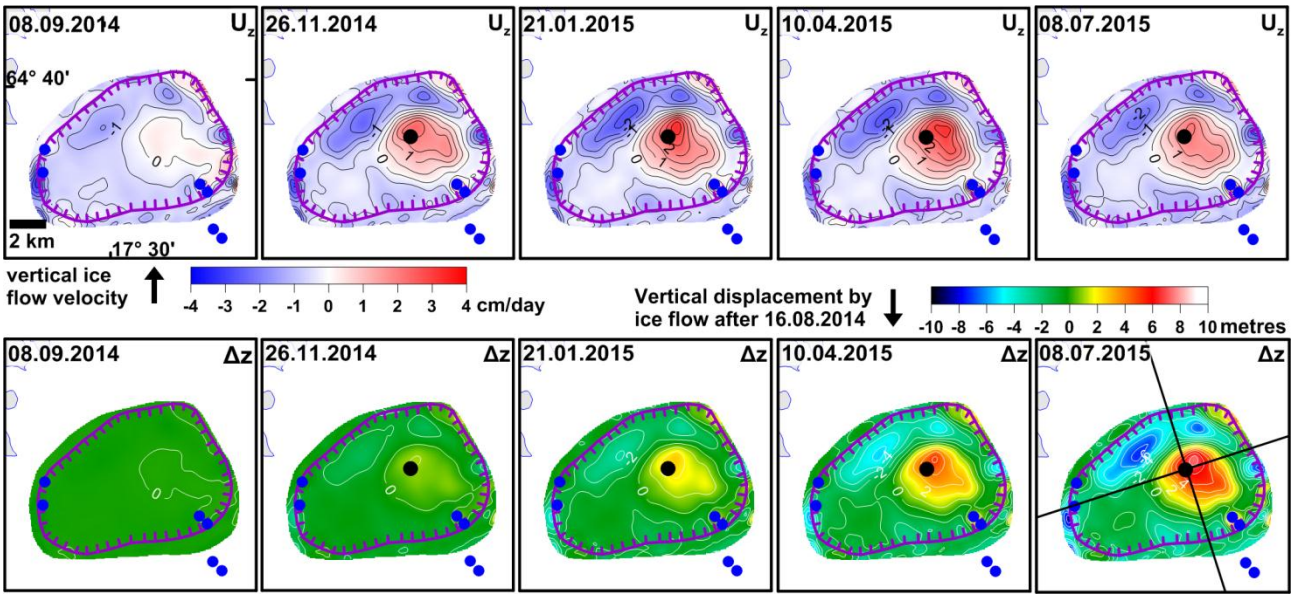

Fig. S2

Results of 3-D Full-Stokes ice flow models (see Materials and Methods) of the response of the glacier within the caldera to the subsidence for five dates spanning the period of collapse. The upper row shows vertical ice flow velocity while the lower row shows the accumulated surface elevation change due to the ice flow for the same dates. The model flow rates are constrained to fit the horizontal displacement of the GPS station BARC in the caldera center from September to February (see Materials and Methods). The maximum vertical ice flow velocity is modelled as having been about 3 cm per day on April 10, 2015. The accumulated uplift for end of eruption on February 27 (Fig. 1C) is obtained by interpolation between January 21 and April 10.

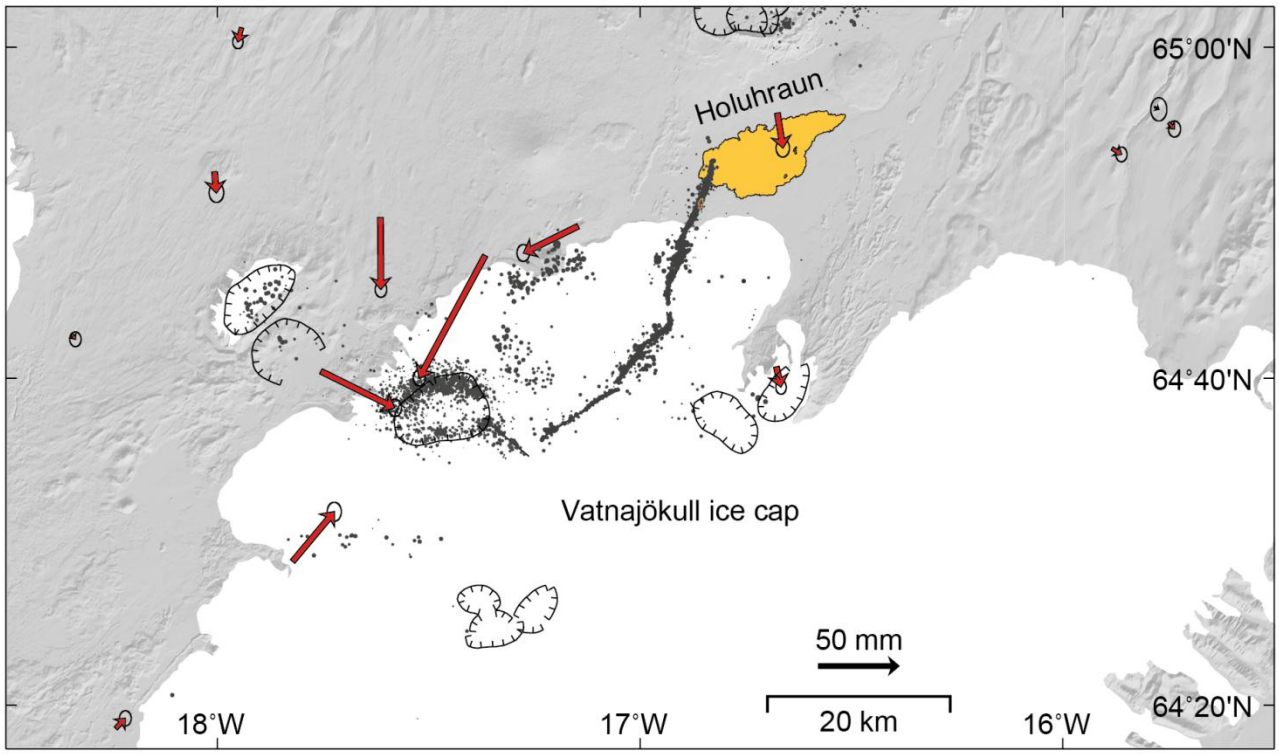

Fig. S3

GPS co-eruptive displacements, spanning September 21, 2014 until February 27, 2015, after the period of dyke opening had ended. The displacement field during the eruption shows consistent movements toward Bárdarbunga caldera suggesting deflation below the caldera. No other major deformation source can be observed during the eruption that can account for significant volume changes. Dots show relatively located earthquakes (20, 24).

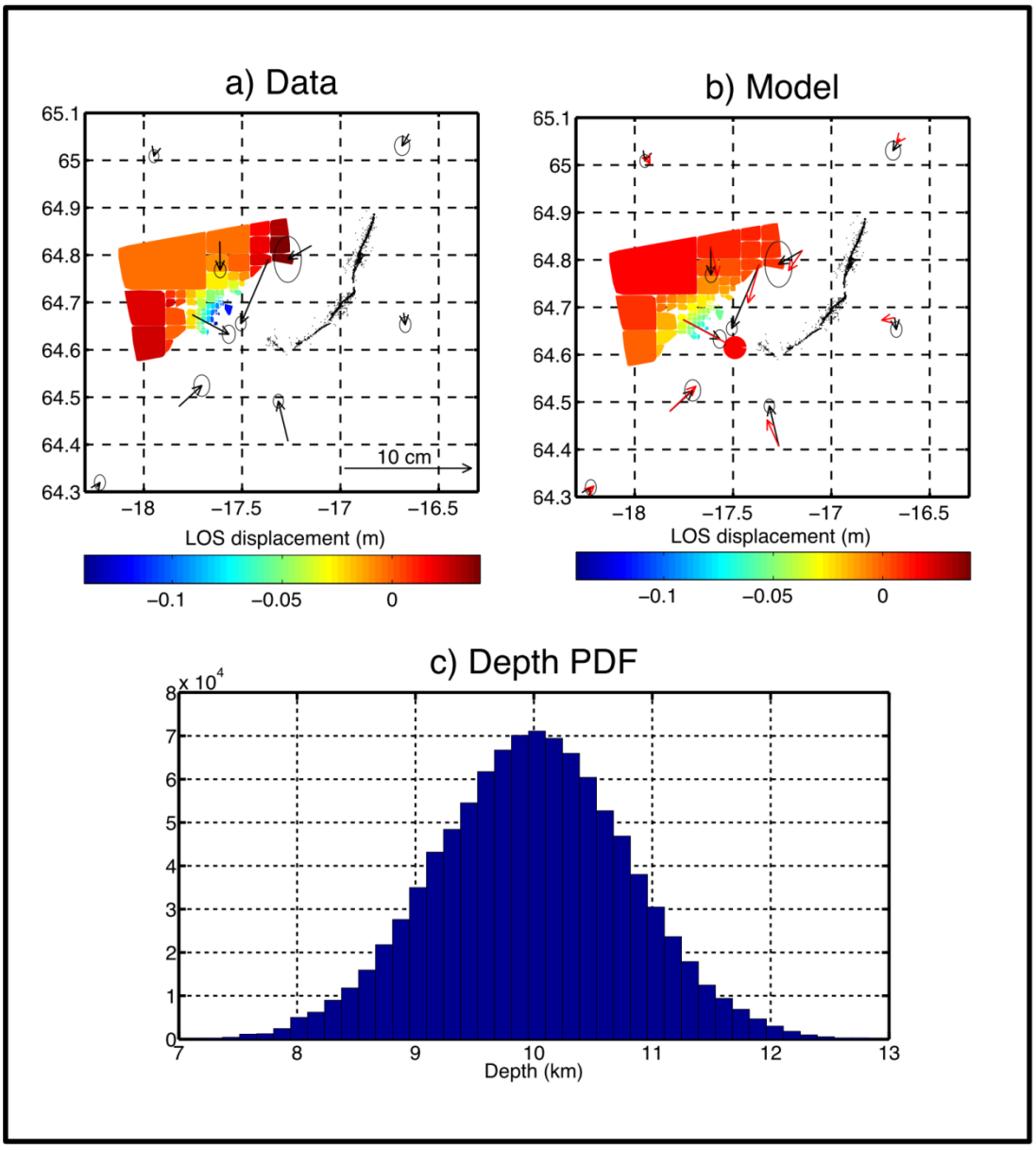

Fig. S4

Geodetic model of regional deformation using a contracting point pressure source. The upper panel from left to right displays the input data (a) and model (b). GPS data in both panels and the CSK ascending interferogram in (a) span the period September 16 to November 7, 2014. The red circle in (b) shows the location of the point pressure source. The black dots represent the seismicity in the vicinity of the dike. The black lines are the inferred dike location. The lower figure (C) displays the probability distribution for depth of the point source from 1 million iterations, using a Markov chain Monte Carlo approach.

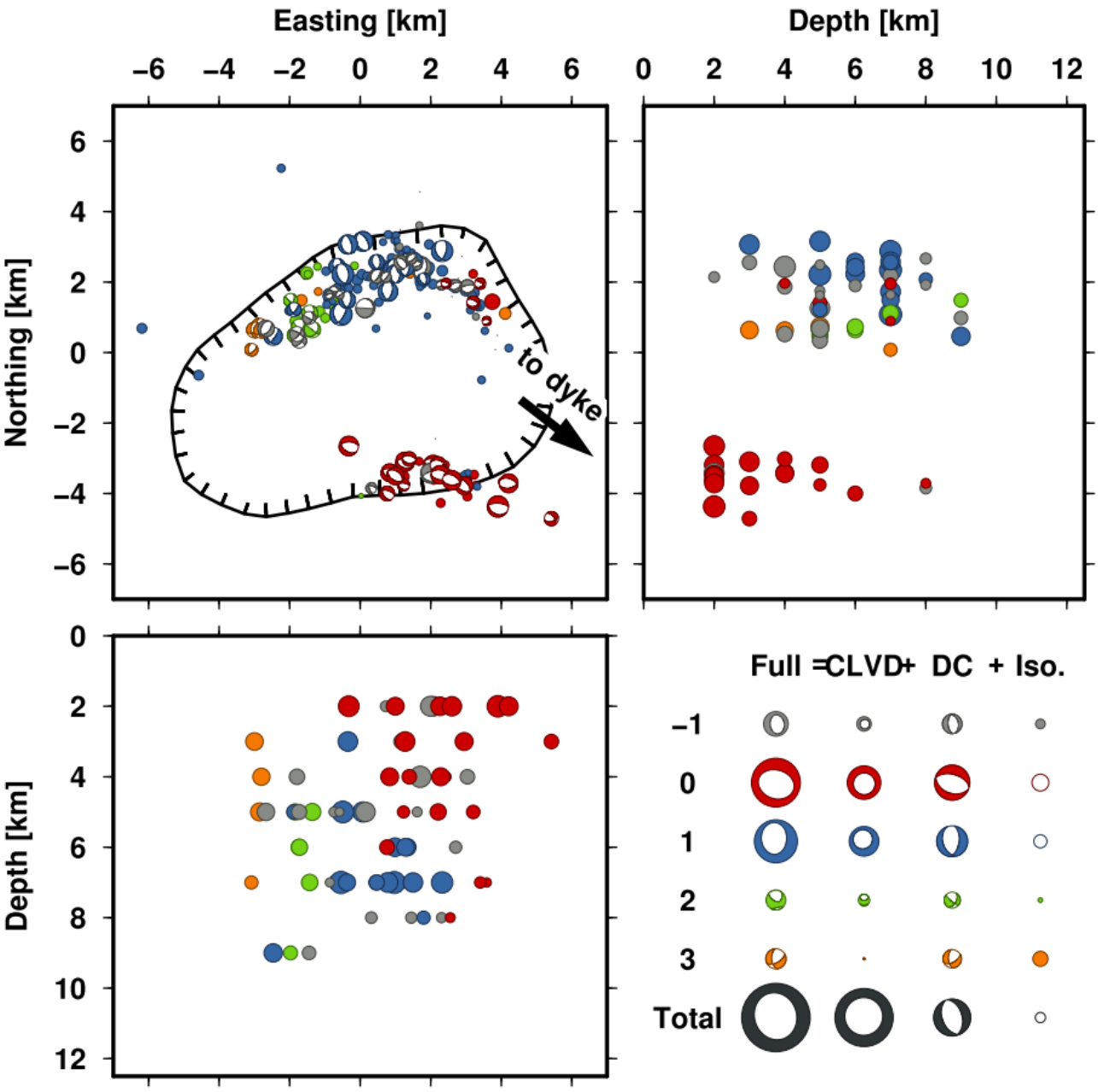

Fig. S5

Source mechanisms of 77 M>5 events. Double couple (DC) components of the retrieved moment tensors (top left) and centroid locations for different cross sections (top right, bottom left). Focal mechanisms are colored according to the result of a DC clustering. The two main clusters are the red cluster, with a WNW-ESE normal faulting component, dominant at the southern rim; and the blue cluster, with N-S oriented normal faulting, characteristic of the northern rim. The standard decomposition is given in the bottom right panel for the four clusters, un-clustered (grey) and cumulative MTs (black).

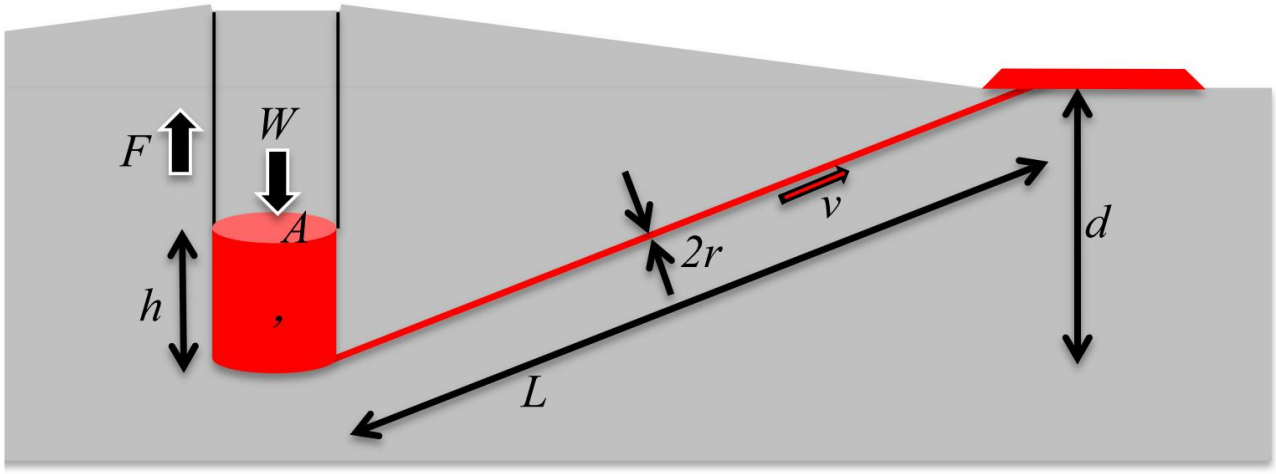

Fig. S6
Schematic of "piston collapse" model. Symbols as described in Materials and Methods

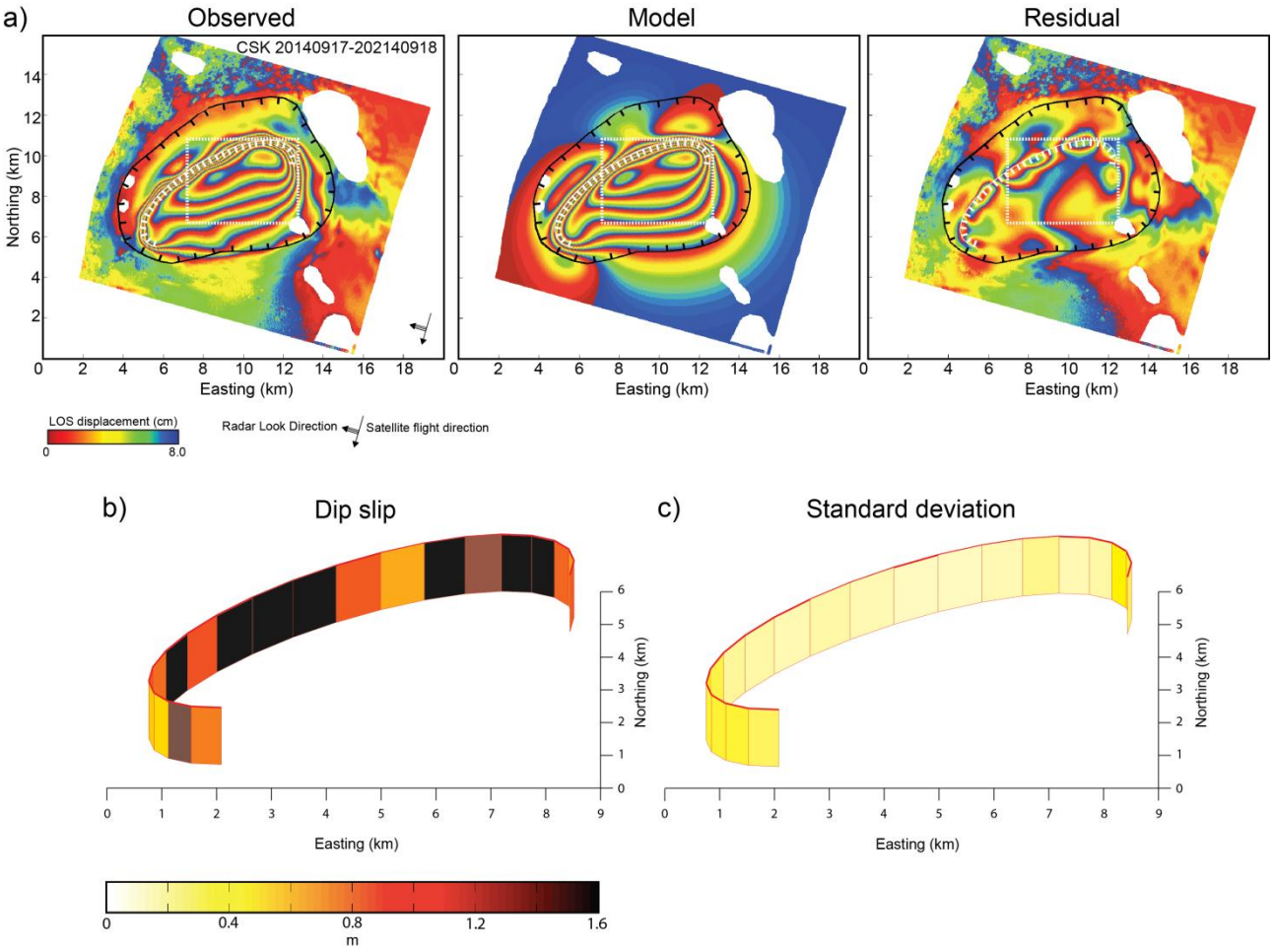

Fig. S7

Fault model for one-day interferogram. The data were acquired by COSMO-SkyMed constellation on 20140917 and 20140918. a) Comparison between observed, predicted and residual surface displacements. The black line outlines the outer caldera rim. The white lines mark the location of the inferred intra-caldera fault system (solid) and of the contracting body (dotted). As no slip is detected on the southern fault in the 24-hour period covered by the interferogram, the southern fault location is not constrained. Cauldrons, for which topography was not well constrained, are masked. b) Median of the posterior probability distribution of dip-slip on vertical fault segments, inferred from modelling. Color indicates the magnitude of slip. c) Standard deviation of the posterior probability distribution, using the same color scale as in b).

Fig. S8

Caldera-dike seismicity correlation. a) Geometry of correlated caldera-dike earthquakes. The dots show all dike earthquakes less than 2.5 km from the dike central line used for Figure 4a. b) Statistics of caldera-dyke earthquake correlations. Rate of dike earthquakes of magnitude $M \geq 0.8$ in time intervals shortly before and after large caldera earthquakes, of size ≥ 4.6, compared with the rate in reference intervals, consisting of all times during the respective period which are at least 3 hours before and at least 3 hours after all $M \geq 4.0$ caldera earthquakes. c) An example of how data was chosen for the analysis (randomly chosen 3 days in October). Upper panel: caldera earthquakes M>4. Lower panel: dike earthquakes during the same period. Blue bins mark three hours before and after caldera earthquakes with M>4.5 used in the study. Yellow bins show data between significant (M>4) caldera earthquakes, used to estimate background seismicity in the dike. Pink shaded bins show data that were not used in the analysis (due to possible overlapping effects).

a

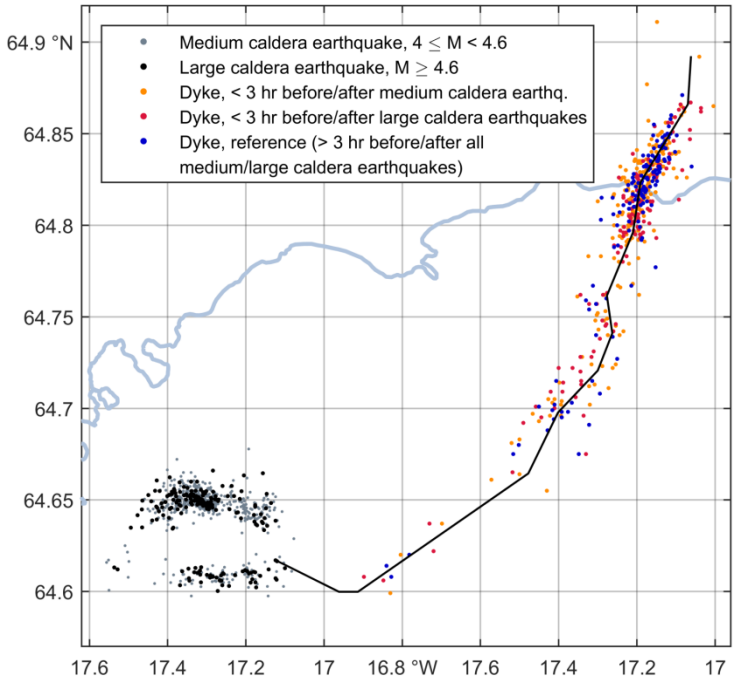

b

Period (2014)	Reference time, total days	Reference rate in dyke (earthq./hr.)	No. of M ≥ 4.6 earthquakes in caldera	Intervals 0–3 hours before M ≥ 4.6 caldera earthquakes			Intervals 0–3 hours after M ≥ 4.6 caldera earthquakes		
				Total hours	No. of eq. in dyke	Rate (eq./hr.)	Total hours	No. of eq. in dyke	Rate (eq./hr.)
01–06 Sept.	3.1	7.04	8	19	132	6.85	19	140	7.26
07–12 Sept.	2.6	2.58	11	30	66	2.20	30	67	2.23
13–18 Sept.	3.1	1.39	9	21	30	1.40	21	27	1.26
19–24 Sept.	2.6	0.85	10	28	26	0.94	28	21	0.76
25–30 Sept.	1.3	0.47	10	29	23	0.81	29	20	0.70
Oct. 2014	5.0	0.14	74	179	44	0.25	179	47	0.26
Nov. 2014	4.2	0.14	25	64	19	0.30	64	12	0.19
Dec. 2014	11.0	0.09	15	42	5	0.12	42	3	0.07
Jan. 2015	14.8	0.19	13	39	10	0.26	39	9	0.23
1–21 Feb. 2015	18.6	0.10	3	9	1	0.11	9	3	0.33

c

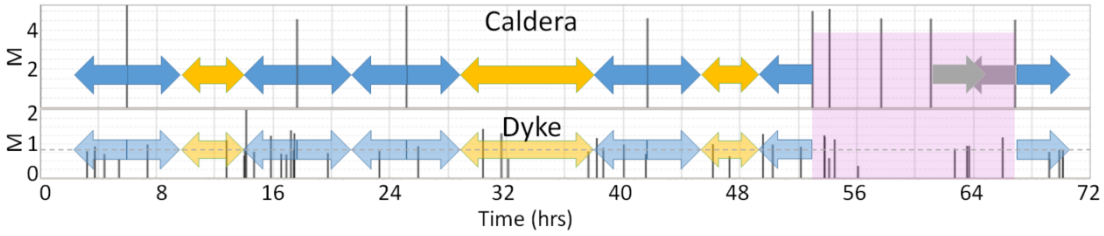

References

1. M. Branney, V. Acocella, in *The Encyclopedia of Volcanoes*, H. Sigurdsson, B. Houghton, H. Rymer, Eds. (Academic Press, Academic Press, Heidelberg, Amsterdam, Boston, ed. 2, 2015), pp. 229–315.

2. J. Stix, T. Kobayashi, Magma dynamics and collapse mechanisms during four historic caldera-forming events. *J. Geophys. Res.* **113**, B09205 (2008). doi:10.1029/2007JB005073

3. A. R. McBirney, A historical note on the origin of calderas. *J. Volcanol. Geotherm. Res.* **42**, 303–306 (1990). doi:10.1016/0377-0273(90)90006-2

4. R. S. J. Sparks, P. W. Francis, R. D. Hamer, R. J. Pankhurst, L. O. O'Callaghan, R. S. Thorpe, R. Page, Ignimbrites of the Cerro Galán caldera, NW Argentina. *J. Volcanol. Geotherm. Res.* **24**, 205–248 (1985). doi:10.1016/0377-0273(85)90071-X

5. T. H. Druitt, R. S. J. Sparks, On the formation of calderas during ignimbrite eruptions. *Nature* **310**, 679–681 (1984). doi:10.1038/310679a0

6. P. W. Lipman, Subsidence of ash-flow calderas: Relation to caldera size and magma-chamber geometry. *Bull. Volc* **59**, 198–218 (1997). doi:10.1007/s004450050186

7. V. Acocella, Understanding caldera structure and development: An overview of analogue models compared to natural calderas. *Earth Sci. Rev.* **85**, 125–160 (2007). doi:10.1016/j.earscirev.2007.08.004

8. O. Roche, T. H. Druitt, O. Merle, Experimental study of caldera formation. *J. Geophys. Res.* **105**, 395–416 (2000). doi:10.1029/1999JB900298

9. T. Simkin, K. A. Howard, Caldera collapse in the Galapagos Islands, 1968: The largest known collapse since 1912 followed a flank eruption and explosive volcanism within the caldera. *Science* **169**, 429–437 (1970). Medline doi:10.1126/science.169.3944.429

10. S. A. Fedotov, Y. K. Markhinin, *The Great Tolbachik Fissure Eruption. Geological and Geophysical Data 1975-1976* (Cambridge Univ. Press, Cambridge, 2011).

11. N. Geshi, T. Shimano, S. Chiba, S. Nakada, Caldera collapse during the 2000 eruption of Miyakejima Volcano, Japan. *Bull. Volcanol.* **64**, 55–68 (2002). doi:10.1007/s00445-001-0184-z

12. T. Staudacher, V. Ferrazzini, A. Peltier, P. Kowalski, P. Boissier, P. Catherine, F. Lauret, F. Massin, The April 2007 eruption and the Dolomieu crater collapse, two major events at Piton de la Fournaise (La Réunion Island, Indian Ocean). *J. Volcanol. Geotherm. Res.* **184**, 126–137 (2009). doi:10.1016/j.jvolgeores.2008.11.005

13. E. P. Holohan, M. P. J. Schöpfer, J. J. Walsh, Stress evolution during caldera collapse. *Earth Planet. Sci. Lett.* **421**, 139–151 (2015). doi:10.1016/j.epsl.2015.03.003

14. K. V. Cashman, G. Giordano, Calderas and magma reservoirs. *J. Volcanol. Geotherm. Res.* **288**, 28–45 (2014). doi:10.1016/j.jvolgeores.2014.09.007

15. J. Battaglia, C. H. Thurber, J.-L. Got, C. A. Rowe, R. A. White, Precise relocation of earthquakes following the 15 June 1991 eruption of Mount Pinatubo (Philippines). *J. Geophys. Res.* **109**, B07302 (2004). doi:10.1029/2003JB002959

16. L. Michon, F. Massin, V. Famin, V. Ferrazzini, G. Roult, Basaltic calderas: Collapse dynamics, edifice deformation, and variations of magma withdrawal. *J. Geophys. Res.* **116**, B03209 (2011). doi:10.1029/2010JB007636

17. H. Björnsson, P. Einarsson, Volcanoes beneath Vatnajökull, Iceland: Evidence from radio-echo sounding, earthquakes and jökulhlaups. *Jokull* **40**, 147–148 (1990).

18. M. T. Gudmundsson, T. Högnadóttir, Volcanic systems and calderas in the Vatnajökull region, central Iceland, constraints on crustal structure from gravity data. *J. Geodyn.* **43**, 153–169 (2007). doi:10.1016/j.jog.2006.09.015

19. T. Thordarson, G. Larsen, Volcanism in Iceland in historical time: Volcano types, eruption styles and eruption history. *J. Geodyn.* **43**, 118–152 (2007). doi:10.1016/j.jog.2006.09.005

20. F. Sigmundsson, A. Hooper, S. Hreinsdóttir, K. S. Vogfjörd, B. G. Ófeigsson, E. R. Heimisson, S. Dumont, M. Parks, K. Spaans, G. B. Gudmundsson, V. Drouin, T. Árnadóttir, K. Jónsdóttir, M. T. Gudmundsson, T. Högnadóttir, H. M. Fridriksdóttir, M. Hensch, P. Einarsson, E. Magnússon, S. Samsonov, B. Brandsdóttir, R. S. White, T. Ágústsdóttir, T. Greenfield, R. G. Green, Á. R. Hjartardóttir, R. Pedersen, R. A. Bennett, H. Geirsson, P. C. La Femina, H. Björnsson, F. Pálsson, E. Sturkell, C. J. Bean, M. Möllhoff, A. K. Braiden, E. P. S. Eibl, Segmented lateral dyke growth in a rifting event at Bárðarbunga volcanic system, Iceland. *Nature* **517**, 191–195 (2015). Medline doi:10.1038/nature14111

21. T. Ágústsdóttir, J. Woods, T. Greenfield, R. G. Green, R. S. White, T. Winder, B. Brandsdóttir, S. Steinthórsson, H. Soosalu, Strike-slip faulting during the 2014 Bárðarbunga-Holuhraun dike intrusion, central Iceland. *Geophys. Res. Lett.* **43**, 1495–1503 (2016). 10.1002/2015GL067423

22. S. R. Gíslason, G. Stefánsdóttir, M. A. Pfeffer, S. Barsotti, Th. Jóhannsson, I. Galeczka, E. Bali, O. Sigmarsson, A. Stefánsson, N. S. Keller, A. Sigurdsson, B. Bergsson, B. Galle, V. C. Jacobo, S. Arellano, A. Aiuppa, E. S. Eiríksdóttir, S. Jakobsson, G. H. Gudfinnsson, S. A. Halldórsson, H. Gunnarsson, B. Haddadi, I. Jónsdóttir, Th. Thordarson, M. Riishuus, Th. Högnadóttir, T. Dürig, G. B. M. Pedersen, A. Höskuldsson, M. T. Gudmundsson, Environmental pressure from the 2014–15 eruption of Bárðarbunga volcano, Iceland. *Geochem. Perspect. Lett* **1**, 84–93 (2015). doi:10.7185/geochemlet.1509

23. O. Roche, T. H. Druitt, Onset of caldera collapse during ignimbrite eruptions. *Earth Planet. Sci. Lett.* **191**, 191–202 (2001). doi:10.1016/S0012-821X(01)00428-9

24. Materials and methods are available as supplementary materials on *Science* Online.

25. J. Browning, A. Gudmundsson, Surface displacements resulting from magma-chamber roof subsidence, with application to the 2014-2015 Bardarbunga-Holuhraun volcanotectonic episode in Iceland. *J. Volcanol. Geotherm. Res.* **308**, 82–98 (2015). doi:10.1016/j.jvolgeores.2015.10.015

26. H. Björnsson, *Hydrology of Ice Caps in Volcanic Regions, Rit. 45* (Soc. Sci. Isl., Reykjavík, 1988).

27. E. P. Holohan, V. R. Troll, B. Van Wyk de Vries, J. J. Walsh, T. R. Walter, Unzipping Long Valley: An explanation for vent migration patterns during an elliptical ring fracture eruption. *Geology* **36**, 323–326 (2008). doi:10.1130/G24329A.1

28. E. P. Holohan, T. R. Walter, M. P. Schöpfer, J. J. Walsh, B. van Wyk de Vries, V. R. Troll, Origins of oblique-slip faulting during caldera subsidence. *J. Geophys. Res.* **118**, 1778–1794 (2013). doi:10.1002/jgrb.50057

29. C. T. Clough, H. B. Maufe, E. B. Baley, The cauldron subsidence of Glen-Coe, and the associated igneous phenomena. *Q. J. Soc. Lond.* **65**, 611–678 (1909). doi:10.1144/GSL.JGS.1909.065.01-04.35

30. H. Bathke, M. Nikkhoo, E. P. Holohan, T. R. Walter, Insights into the 3D architecture of an active caldera ring-fault at Tendürek volcano through modeling of geodetic data. *Earth Planet. Sci. Lett.* **422**, 157–168 (2015). doi:10.1016/j.epsl.2015.03.041

31. A. Fichtner, H. Tkalcic, Insights into the kinematics of a volcanic caldera drop: Probabilistic finite-source inversion of the 1996 Bardarbunga, Iceland, earthquake. *Earth Planet. Sci. Lett.* **297**, 607–615 (2010). doi:10.1016/j.epsl.2010.07.013

32. B. Riel, P. Milillo, M. Simons, P. Lundgren, H. Kanamori, S. Samsonov, The collapse of Bárðarbunga Caldera, Iceland. *Geophys. J. Int.* **202**, 446–453 (2015). doi:10.1093/gji/ggv157

33. S. Cesca, A. T. Sen, T. Dahm, Seismicity monitoring by cluster analysis of moment tensors. *Geophys. J. Int.* **196**, 1813–1826 (2014). doi:10.1093/gji/ggt492

34. A. Shuler, G. Ekström, M. Nettles, Physical mechanisms for vertical-CLVD earthquakes at active volcanoes. *J. Geophys. Res.* **118**, 1569–1586 (2013). doi:10.1002/jgrb.50131

35. K. Abe, Seismicity of the caldera-making eruption of Mount Katmai, Alaska in 1912. *Bull. Seismol. Soc. Am.* **82**, 175–191 (1992).

36. C. P. Montagna, H. M. Gonnermann, Magma flow between summit and Pu'u 'O'o at Kilauea Volcano, Hawaii. *Geochem. Geophys. Geosyst.* **14**, 2232–2246 (2013). doi:10.1002/ggge.20145

37. H. Kumagai, T. Ohminato, M. Nakano, M. Ooi, A. Kubo, H. Inoue, J. Oikawa, Very-long-period seismic signals and caldera formation at Miyake Island, Japan. *Sci.* **293**, 687–690 (2001). Medline doi:10.1126/science.1062136

38. G. Wadge, Steady state volcanism: Evidence from eruption histories of polygenetic volcanoes. *J. Geophys. Res.* **87**, 4035–4049 (1982). doi:10.1029/JB087iB05p04035

39. A. Geyer, A. Folch, J. Martí, Relationship between caldera collapse and magma chamber withdrawal: An experimental approach. *J. Volcanol. Geotherm. Res.* **157**, 375–386 (2006). doi:10.1016/j.jvolgeores.2006.05.001

40. A. Folch, J. Marti, Time-dependent chamber and vent conditions during explosive caldera-forming eruptions. *Earth Planet. Sci. Lett.* **280**, 246–253 (2009). doi:10.1016/j.epsl.2009.01.035

41. W. Hildreth, J. Fierstein, Katmai volcanic cluster and the great eruption of 1912. *Geophys. J. Int.* **112**, 446–453 (2000).

42. B. C. Bautista, M. L. P. Bautista, R. S. Stein, E. S. Barcelona, R. S. Punongbayan, E. P. Laguerta, A. R. Rasdas, G. Ambubuyog, E. Q. Amin, in *Fire and Mud: Eruptions and Lahars of Mount Pinatubo, Philippines*, C. G. Newhall, R. S. Punongbayan, Eds. (Philippine

Institute of Volcanology and Seismology & University of Washington Press, Quezon City, Seattle & London, 1996), pp. 351–370.

43. J. Mori, R. A. White, D. H. Harlow, P. Okubo, J. A. Power, R. P. Hoblitt, E. P. Laguerta, A. Lanuza, B. C. Bautista, in *Fire and Mud: Eruptions and Lahars of Mount Pinatubo, Philippines*, C. G. Newhall, R. S. Punongbayan, Eds. (Philippine Institute of Volcanology and Seismology & University of Washington Press, Quezon City, Seattle & London, 1996), pp. 339–350.

44. L. Michon, T. Staudacher, V. Ferrazzini, P. Bachèlery, J. Marti, April 2007 collapse of Piton de la Fournaise: A new example of caldera formation. *Geophys. Res. Lett.* **34**, L21301 (2007). doi:10.1029/2007GL031248

45. F. R. Fontaine, G. Roult, L. Michon, G. Barruol, A. Di Muro, The 2007 eruptions and caldera collapse of the Piton de la Fournaise volcano (La Reunion Island) from tilt analysis at a single very broadband seismic station. *Geophys. Res. Lett.* **41**, 2803–2811 (2014). doi:10.1002/2014GL059691

46. A. Di Muro, N. Metrich, D. Vergani, M. Rosi, P. Armienti, T. Fougeroux, E. Deloule, I. Arienzo, L. Civetta, The shallow plumbing system of Piton de la Fournaise Volcano (La Reunion Island, Indian Ocean) revealed by the major 2007 caldera-forming eruption. *J. Petrol.* **55**, 1287–1315 (2014). doi:10.1093/petrology/egu025

47. T. Kaneko, A. Yasuda, T. Shimano, S. Nakada, T. Fujii, T. Kanazawa, A. Nishizawa, Y. Matsumoto, Submarine flank eruption preceding caldera subsidence during the 2000 eruption of Miyakejima Volcano, Japan. *Bull. Volcanol.* **67**, 243–253 (2005). doi:10.1007/s00445-004-0407-1

48. M. Amma-Miyasaka, M. Nakagawa, S. Nakada, Magma plumbing system of the 2000 eruption of Miyakejima Volcano, Japan. *Bull. Volcanol.* **67**, 254–267 (2005). doi:10.1007/s00445-004-0408-0

49. T. Nishimura, S. Ozawa, M. Murakami, T. Sagiya, T. Tada, M. Kaidzu, M. Ukawa, Crustal deformation caused by magma migration in the northern Izu Islands, Japan. *Geophys. Res. Lett.* **28**, 3745–3748 (2001). doi:10.1029/2001GL013051

50. S. A. Fedotov, L. B. Slavina, S. L. Senyukov, M. S. Kuchay, Seismic processes and migration of magma during the Great Tolbachik Fissure Eruption of 1975-1976 and Tolbachik Fissure Eruption of 2012-2013, Kamchatka Peninsula. *Izv. Atmos. Ocean. Phys.* **51**, 667–687 (2015). doi:10.1134/S000143381507004X

51. S. A. Fedotov, I. S. Utkin, L. I. Utkina, The peripheral magma chamber of Ploskii Tolbachik, a Kamchatka basaltic volcano: Activity, location and depth, dimensions, and their changes based on magma discharge observations. *J. Volcanol. Seismol.* **5**, 369–385 (2011). doi:10.1134/S0742046311060042

52. P. Doubik, B. E. Hill, Magmatic and hydromagmatic conduit development during the 1975 Tolbachik Eruption, Kamchatka, with implications for hazards assessment at Yucca Mountain, NV. *J. Volcanol. Geotherm. Res.* **91**, 43–64 (1999). doi:10.1016/S0377-0273(99)00052-9

53. S. A. Fedotov, A. M. Chirkov, N. A. Gusev, G. N. Kovalev, Y. B. Slezin, The large fissure eruption in the region of Plosky Tolbachik volcano in Kamchatka, 1975–1976. *Bull. Volcanol.* **43**, 47–60 (1980). doi:10.1007/BF02597610

54. J. Filson, T. Simkin, L. K. Leu, Seismicity of a caldera collapse: Galapagos Islands 1968. *J. Geophys. Res.* **78**, 8591–8622 (1973). doi:10.1029/JB078i035p08591

55. J. E. Hammer, M. J. Rutherford, W. Hildreth, Magma storage prior to the 1912 eruption at Novarupta, Alaska. *Contrib. Mineral. Petrol.* **144**, 144–162 (2002). doi:10.1007/s00410-002-0393-2

56. M. J. Rutherford, J. D. Devine, in *Fire and Mud: Eruptions and Lahars of Mount Pinatubo, Philippines*, C. G. Newhall, R. S. Punongbayan, Eds. (Philippine Institute of Volcanology and Seismology & University of Washington Press, Quezon City, Seattle & London, 1996), pp. 751–766.

57. H. Kanamori, J. Mori, E. Hauksson, T. H. Heaton, L. K. Hutton, L. M. Jones, Determination of earthquake energy release and ML using TERRAscope. *Bull. Seismol. Soc. Am.* **83**, 330–346 (1993).

58. M. Kikuchi, Y. Yamanaka, K. Koketsu, Source process of the long-period seismic pulses associated with the 2000 eruption of Miyakejima volcano and its implications. *J. Geograph. Tokyo* **110**, 204–216 (2001). doi:10.5026/jgeography.110.2_204

59. M. T. Gudmundsson, T. Höganadóttir, A. B. Kristinsson, S. Gudbjornsson, Geothermal activity in the subglacial Katla caldera, Iceland 1999-2005, studied with radar altimetry. *Ann. Glaciol.* **45**, 66–72 (2007). doi:10.3189/172756407782282444

60. C. Mätzler, Microwave permittivity of dry snow. *IEEE Trans. Geosci. Rem. Sens.* **34**, 573–581 (1996). doi:10.1109/36.485133

61. C. Rossi, C. Minet, T. Fritz, M. Eineder, R. Bamler, Temporal monitoring of subglacial volcanoes with TanDEM-X—Application to the 2014–2015 eruption within the Bárðarbunga volcanic system, Iceland. *Remote Sens. Environ.* **181**, 186–197 (2016). doi:10.1016/j.rse.2016.04.003

62. T. Jóhannesson, H. Björnsson, E. Magnússon, S. Guðmundsson, F. Pálsson, O. Sigurðsson, T. Thorsteinsson, E. Berthier, Ice-volume changes, bias estimation of mass-balance measurements and changes in subglacial lakes derived by lidar mapping of the surface of Icelandic glaciers. *Ann. Glaciol.* **54**, 63–74 (2013). doi:10.3189/2013AoG63A422

63. E. Magnusson, F. Palsson, H. Bjornsson, S. Gudmundsson, Removing the ice cap of Oraefajokull central volcano, SE-Iceland: Mapping and interpretation of bedrock topography, ice volumes, subglacial troughs and implications for hazards assessments. *Jokull* **62**, 131–150 (2012).

64. H. Bjornsson, F. Pálsson, M. T. Gudmundsson, *Vatnajokull, Northwest Part, 1:100 000: Bedrock topography* (Landsvirkjun and Science Institute, University of Iceland, 1992)

65. A. H. Jarosch, Icetools: A full Stokes finite element model for glaciers. *Comput. Geosci.* **34**, 1005–1014 (2008). doi:10.1016/j.cageo.2007.06.012

66. J. W. Glen, The creep of polycrystalline ice. *P. Roy. Soc. A-Math. Phys.* **228**, 519–538 (1955). doi:10.1098/rspa.1955.0066

67. K. M. Cuffey, W. S. B. Paterson, *The Physics of Glaciers* (Elsevier Butterworth-Heinemann, Burlington, ed. 4, 2010).

68. C. E. Lesher, F. J. Spera, in *The Encyclopedia of Volcanoes*, H. Sigurdsson, B. Houghton, H. Rymer, Eds. (Academic Press, Heidelberg, Amsterdam, Boston, ed. 2, 2015), pp. 113–141.

69. R. Bödvarsson, S. T. Rögnvaldsson, R. Slunga, E. Kjartansson, The SIL data acquisition system—at present and beyond year 2000. *Phys. Earth Planet. Inter.* **113**, 89–101 (1999). doi:10.1016/S0031-9201(99)00032-1

70. R. Slunga, S. T. Rögnvaldsson, R. Bödvarsson, Absolute and relative locations of similar events with application to microearthquakes in southern Iceland. *Geophys. J. Int.* **123**, 409–419 (1995). doi:10.1111/j.1365-246X.1995.tb06862.x

71. S. Th. Rögnvaldsson, R. Slunga, Routine fault plane solutions for local networks: A test with synthetic data. *Bull. Seismol. Soc. Am.* **83**, 1232–1247 (1993).

72. R. Stefánsson, R. Böđvarsson, R. Slunga, P. Einarsson, S. Jakobsdóttir, H. Bungum, S. Gregersen, J. Havskov, J. Hjelme, H. Korhonen, Earthquake prediction research in the South Iceland seismic zone and the SIL project. *Bull. Seismol. Soc. Am.* **83**, 696–716 (1993).

73. S. Cesca, A. Rohr, T. Dahm, Discrimination of induced seismicity by full moment tensor inversion and decomposition. *J. Seismol.* **17**, 147–163 (2013). http://doi.org/10.1007/s10950-012-9305-8

74. P. A. Rosen, S. Hensley, I. R. Joughin, F. K. Li, S. N. Madsen, E. Rodriguez, R. M. Goldstein, Synthetic aperture radar interferometry, presented at *Proceedings of the IEEE,* 2000.

75. B. Kampes, Delft Object-oriented Radar Interferometric Software: User's Manual and Technical Documentation v4.02, presented at *Delft Technical University*, 1999.

76. Y. Y. Kagan, 3-D rotation of double-couple earthquake sources. *Geophys. J. Int.* **106**, 709–716 (1991). doi:10.1111/j.1365-246X.1991.tb06343.x

77. R. M. Goldstein, C. L. Werner, Radar interferogram filtering for geophysical applications. *Geophys. Res. Lett.* **25**, 4035–4038 (1998). doi:10.1029/1998GL900033

78. C. W. Chen, H. A. Zebker, Two-dimensional phase unwrapping with use of statistical models for cost functions in nonlinear optimization. *J. Opt. Soc. Am. A Opt. Image Sci. Vis.* **18**, 338–351 (2001). Medline doi:10.1364/JOSAA.18.000338

79. Y. Okada, Internal deformation due to shear and tensile faults in a half-space. *Bull. Seismol. Soc. Am.* **82**, 1018–1040 (1992).

80. A. Hooper, J. Pietrzak, W. Simons, H. Cui, R. Riva, M. Naeije, A. Terwisscha van Scheltinga, E. Schrama, G. Stelling, A. Socquet, Importance of horizontal seafloor motion on tsunami height for the 2011 M_w=9.0 Tohoku-Oki earthquake. *Earth Planet. Sci. Lett.* **361**, 469–479 (2013). doi:10.1016/j.epsl.2012.11.013

81. C. E. Ford, D. G. Russell, J. A. Craven, M. R. Fisk, Olivine-liquid equilibria: Temperature, pressure and composition dependence of the crystal/liquid cation partition coefficients for Mg, $Fe2^{+}$, Ca and Mn. *J. Petrol.* **24**, 256–266 (1983). doi:10.1093/petrology/24.3.256

82. H. J. Yang, R. J. Kinzler, T. L. Grove, Experiments and models of anhydrous, basaltic olivine-plagioclase-augite saturated melts from 0.001 to 10 kbar. *Contrib. Mineral. Petrol.* **124**, 1–18 (1996). doi:10.1007/s004100050169

83. G. H. Gudfinnsson, D. C. Presnall, A pressure-independent geothermometer for primitive mantle melts. *J. Geophys. Res.* **106**, 16205–16211 (2001). doi:10.1029/2000JB000066

84. K. D. Putirka, Thermometers and barometers for volcanic systems. *Rev. Mineral. Geochem.* **69**, 61–120 (2008). doi:10.2138/rmg.2008.69.3

85. Y. Kawakami, J. Yamamoto, H. Kagi, Micro-Raman densimeter for CO2 inclusions in mantle-derived minerals. *Appl. Spectrosc.* **57**, 1333–1339 (2003). Medline doi:10.1366/000370203322554473

86. M. Burton, P. Allard, F. Muré, A. La Spina, Magmatic gas composition reveals the source depth of slug-driven strombolian explosive activity. *Science* **317**, 227–230 (2007).http://www.ncbi.nlm.nih.gov/entrez/query.fcgi?cmd=Retrieve&db=PubMed&list_uids=17626881&dopt=Abstract doi:10.1126/science.1141900

87. A. Aiuppa, C. Federico, G. Giudice, S. Gurrieri, Chemical mapping of a fumarolic field: La Fossa Crater, Vulcano Island (Aeolian Islands, Italy). *Geophys. Res. Lett.* **32**, L13309 (2005). doi:10.1029/2005GL023207

88. P.-J. Gauthier, O. Sigmarsson, M. Gouhier, B. Haddadi, S. Moune, Elevated gas flux and trace metal degassing from the 2014–2015 fissure eruption at the Bárðarbunga volcanic system, Iceland. *J. Geophys. Res. Solid Earth* **121**, 1610–1630 (2016). 10.1002/2015JB012111

89. E. Bali, O. Sigmarsson, S. Jakobsson, H. Gunnarsson, Volatile budget of the Nornahraun eruption in the Bárðarbunga system, Iceland. Geophysical Research Abstracts Vol. 17, EGU2015-5757, 2015 EGU General Assembly (2015). http://meetingorganizer.copernicus.org/EGU2015/EGU2015-5757.pdf

90. A. Burgisser, M. Alletti, B. Scaillet, Simulating the behavior of volatiles belonging to the C–O–H–S system in silicate melts under magmatic conditions with the software D-Compress. *Comput. Geosci.* **79**, 1–14 (2015). doi:10.1016/j.cageo.2015.03.002

91. D. O. Potyondy, P. A. Cundall, A bonded particle model for rock. *Int. J. Rock Mech. Min.* **41**, 1329–1364 (2004). doi:10.1016/j.ijrmms.2004.09.011

92. D. Mas Ivars, M. E. Pierce, C. Darcel, J. Reyes-Montes, D. O. Potyondy, R. P. Young, P. A. Cundall, The synthetic rock mass approach for jointed rock mass modelling. *Int. J. Rock Mech. Min* **48**, 219–244 (2011). doi:10.1016/j.ijrmms.2010.11.014

93. Itasca Consulting Group, Inc., *PFC2D - Particle Flow Code in Two-Dimensions, Ver. 5.0* (Minneapolis, Itasca, 2014).

94. K. Mogi, Relations between the eruptions of various volcanoes and the deformations of the ground surfaces around them. *Bull. Earthq. Res. Inst. Univ. Tokyo* **36**, 99–134 (1958).

95. M. Ripepe, D. D. Donne, R. Genco, G. Maggio, M. Pistolesi, E. Marchetti, G. Lacanna, G. Ulivieri, P. Poggi, Volcano seismicity and ground deformation unveil the gravity-driven magma discharge dynamics of a volcanic eruption. *Nat. Commun.* **6**, 6998 (2015). Medline doi:10.1038/ncomms7998

96. Y. Bottinga, D. Weill, The viscosity of magmatic silicate liquids: A model for calculation. *Am. J. Sci.* **272**, 438–475 (1972). doi:10.2475/ajs.272.5.438